Chemical Science

EDGE ARTICLE

View Article Online
View Journal | View Issue

Cite this: *Chem. Sci.*, 2017, **8**, 6149

Thermochemical functionalisation of graphenes with minimal framework damage†

Sheng Hu,[a] Zachary P. L. Laker,[b] Hannah S. Leese,[a] Noelia Rubio,[a] Martina De Marco,[a] Heather Au,[a] Mark S. Skilbeck,[b] Neil R. Wilson[b] and Milo S. P. Shaffer*[a]

Received 21st December 2016
Accepted 15th June 2017

DOI: 10.1039/c6sc05603b

rsc.li/chemical-science

Graphene and graphene nanoplatelets can be functionalised *via* a gas-phase thermochemical method; the approach is versatile, readily scalable, and avoids the introduction of additional defects by exploiting existing sites. Direct TEM imaging confirmed covalent modification of single layer graphene, without damaging the connectivity of the lattice, as supported by Raman spectrometry and AFM nano-indentation measurements of mechanical stiffness. The grafting methodology can also be applied to commercially-available bulk graphene nanoplatelets, as illustrated by the preparation of anionic, cationic, and non-ionic derivatives. Successful bulk functionalisation is evidenced by TGA, Raman, and XPS, as well as in dramatic changes in aqueous dispersability. Thermochemical functionalisation thus provides a facile approach to modify both graphene monolayers, and a wide range of graphene-related nanocarbons, using variants of simple CVD equipment.

Introduction

Graphene and related materials, including few-layer graphene, graphene oxide, and graphene nanoplatelets (GNPs), have attracted considerable attention due to the promise of their thermal, electrical, mechanical and many other unique properties.[1–3] While some applications can use the materials in their as-received forms, many others require chemical modification, for example, to control properties such as solubility[4] and interfacial adhesion,[5,6] or to introduce specific functional benefits such as catalytic activity, fluorescence, analyte binding, *etc.*[7,8] However, most covalent functionalisation routes introduce damage that impairs the intrinsic properties of graphene.[9–11] Often, harsh oxidation conditions are used to introduce oxygen-containing functional groups which are used for further derivatisation.[12] Oxidation routes create high levels of carbon framework damage, seriously degrading the intrinsic properties of interest; whilst a variety of processes remove some excess oxygen-groups, the original properties are only partially recovered even on annealing at temperatures over 1000 °C.[13,14] Less damaging routes can be used to modify the surface without etching the carbon framework. For example, reduction by alkali metals can generate soluble graphenides that can react with a range of electrophiles to yield grafted products.[15] However, the reaction conditions can be demanding, and work-up of liquid phase reactions on nanomaterials is typically slow. In addition, even modest levels (1–3 at%) of direct addition reactions can destroy the characteristic graphene band structure.[16] Solvent-free or gas-phase methods are typically simple, scalable processes, offering a high degree of cleanliness, with minimal work-up. Conventional gas-phase modification routes range from thermal reduction of graphene oxide under inert gas atmosphere,[17,18] to plasma oxidation (now commercialized),[19] and microwave irradiation treatments.[20,21] Gas phase reactions avoid the effects of capillary collapse that drive unwanted restacking particularly of single layer graphenes or 3D structured graphene-related (hybrid) materials.

Previously, we developed a self-limiting, scalable, thermochemical functionalisation method and demonstrated its applicability to multi-walled carbon nanotubes (MWCNTs),[22,23] and carbon black nanoparticles (CB NPs),[24] with a wide range of functionalizing moieties. The mechanism involves the thermal decomposition of pre-existing defect groups to generate surface radicals which are able to graft many different reagents; since only existing sites are activated, it is hypothesised that additional damage to the carbon framework is avoided. It is feasible to implement this process in an entirely solvent-free set-up, as long as the grafting reagent is sufficiently volatile to be introduced, and the excess removed, by vacuum. The approach typically introduces only a low degree of functionalisation, at pre-existing defect sites, and hence does not intrinsically degrade the original as-synthesised framework properties; nevertheless, these low levels of functionalization have been shown to be sufficient to adjust wetting and dispersibility as required. Herein, the approach was extended to single layer graphene (SLG) to confirm the generality of the approach and

[a]*Department of Chemistry and London Centre for Nanotechnology, Imperial College London, London SW7 2AZ, UK. E-mail: m.shaffer@imperial.ac.uk*

[b]*Department of Physics, University of Warwick, Coventry CV4 7AL, UK*

† Electronic supplementary information (ESI) available. See DOI: 10.1039/c6sc05603b

explore the effects on the graphene lattice in detail. By using graphene supported on a transmission electron microscopy (TEM) grid, it is possible to directly image the grafted functionalities, and explicitly measure the effects on mechanical performance. The use of a gas phase approach is particularly helpful for maintaining the cleanliness needed for high resolution imaging, as well as representing a generic, clean, route for functionalisation of CVD graphene on substrates. Having established efficacy on single monolayers, the approach was applied to the functionalisation of bulk quantities of GNPs, enabling different types of characterisation, and highlighting the versatility of the approach. The gas phase approach is not expected to exfoliate individual layers, rather modify the accessible surface of SLG/GNP materials.

Results and discussion

The pristine graphene grids or GNP powders were processed in their as-received form, by heating the materials under vacuum (*ca.* 10^{-5} mbar). Although a range of activation temperatures have been explored, the thermochemical activation is usually performed at 1000 °C;[22–24] however, the single-layer graphene TEM grid, was only heated to 850 °C, to avoid damaging the silicon nitride support used for subsequent mechanical measurements. The activated graphene/GNPs were then cooled to room temperature, before exposure to grafting reagents (refer to Scheme 1). For the graphene grid study, a small, rigid, volatile grafting agent was selected: 1,1,1-trifluoro-2-iodoethane (TFI); the corresponding functionalised sample is labelled as TFI-SLG. In addition, a thermally-treated control sample (TTC-SLG) was prepared with the identical activation protocol but followed by exposure to air rather than TFI, after cooling to ambient temperature (refer to Fig. 1a and b). The high-resolution TEM (HR-TEM) images of TFI-SLG (Fig. 1c and d) showed distinctive features, attributed to the grafted TFI molecules, by comparison to multi-slice TEM image simulations,[25] based on the experimental imaging conditions. Interestingly, the imaged functionalities did not degrade or move laterally across the graphene, during moderate exposure to the beam. Instead,

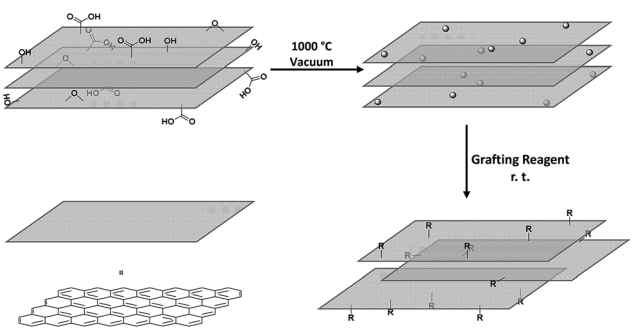

Scheme 1 Reaction scheme for the thermochemical functionalisation of few-layer graphene (nanoplatelets) by heating the pristine material to 1000 °C under vacuum (10^{-4} mbar), during which process the radicals (●) were generated, followed by exposure to grafting reagents (–R) at ambient temperature.

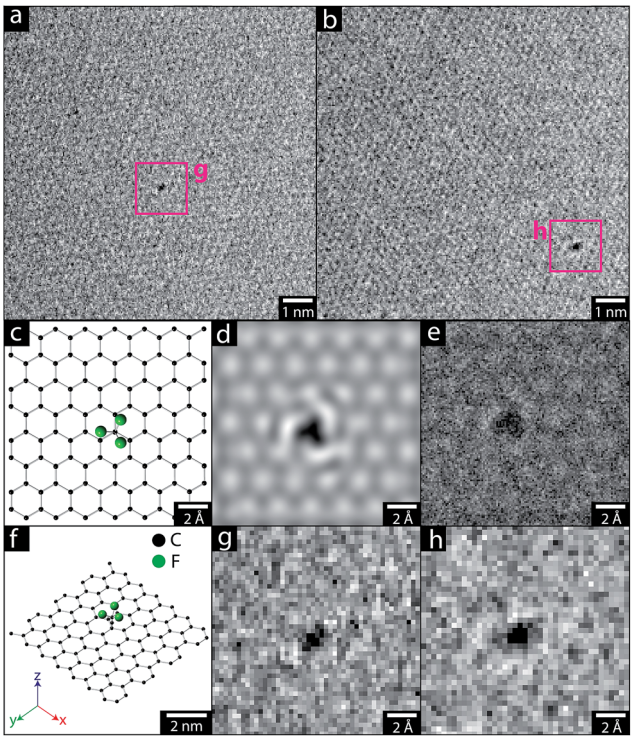

Fig. 1 HRTEM results showing presence of functionalities on graphene. (a), (b) HRTEM images show localised high-contrast functionalities on graphene surface. (c), (f) Model used for multislice simulations plan and perspective views. (d), (e) Multislice simulations of functional group modelled using perfect and experimentally-measured noise. (g), (h) Magnified regions-of-interest from (a), (b) displaying similar appearance and contrast to the realistic multislice simulation presented in (e).

some motion (likely rotation) about the bonding site was visible, as shown in the movies presented in the ESI.† This behavior suggests a covalent bond at a defined site. These features appeared on the TFI-G surface, with an approximate concentration of 1×10^{-3} nm^{-2}, but were not observed on the TTC-SLG control. The equivalent grafting concentration, defined by the graphitic carbon to TFI site ratio (C/R), can be estimated to be 38 000 : 1, by normalising the grafting site concentration to atomic areal density of graphene (5.246×10^{-2} nm^2 per two carbon atoms). The value is seemingly low, compared to previous results on multi-walled carbon nanotubes (MWCNTs, 1000 : 1)[23] and carbon black nanoparticles (CB NPs, 250 : 1).[24] However, the high quality of the graphene used means that the concentration of initial defect sites available for activation is low. This low defect concentration is observed in the TEM images of the TTC-SLG and shown by the low intensity or even complete absence of a D band in Raman spectrum of either the TTC- or the functionalised SLG (ESI Fig. S1†). Furthermore, the functional groups could only be clearly identified when present as individual species against clean, perfect regions of the graphene lattice. Thus the contribution from grafting occurring at larger defects, grain boundaries, or in clusters are not included, though expected to be significant. The lower activation temperature (850 °C) can also reduce the

grafting ratio slightly but is unlikely to be the dominant effect, since the grafting ratio on CNTs was only halved by this change in temperature.[26] Overall, the low grafting density on the highly perfect SLG surface, and high quality of the structure after grafting is consistent with the proposed defect-initiated mechanism.

AFM nano-indentation was used to measure the mechanical properties of the functionalised graphene sheet, using an established method.[27] As shown in Table 1 (and ESI Fig. S2†), neither the thermochemical treatment (TTC-SLG) nor the functionalization (TFI-SLG) changed the Young's modulus, measurably, compared to the pristine graphene grid (AR-SLG).

Whilst the very dilute modification of high quality monolayer graphene helped to identify covalent binding of the functional groups, the low surface concentration and absolute quantity preclude further chemical measurements. The functionalisation was, therefore, extended to typical bulk GNPs with high surface area, synthesised by a non-oxidising chemical growth process. SEM images of the initial GNP powders (Fig. 2a) showed stacks of flake structures, as further confirmed by TEM and AFM of GNPs deposited from dispersions (Fig. 2b and c). The lateral average size of the GNPs used here was estimated to be 2.4 ± 2.1 μm from image analysis (histogram available in ESI Fig. S5†).

The typical thickness of the GNPs, as determined by AFM was approximately 4 nm (refer to Fig. 2d), indicating around 10 graphitic layers; bulk XRD data gave similar values, 5–6 nm (see ESI, Fig. S4 & Table S2†). The GNPs have a high defect concentration, as shown by their waviness, small size, large I_D/I_G ratio in Raman spectra (0.97 ± 0.27) and high oxygen content determined by XPS (refer to Table 2). A series of functionalities that have been proved suitable for thermochemical functionalisation reactions on MWCNTs and CB NPs[23,24] were used again for the GNP grafting, including the polymerisable monomers methyl methacrylate (MMA), 4-vinyl pyridine (4VP) and poly (ethylene glycol)methyl acrylate (PEGMA), as well as 1-iododecane (IDD) as a non-polymerisable reference. A thermally-treated control sample (TTC-GNPs) was also prepared as a baseline for the functionalised GNPs (f-GNPs).

TGA was employed to quantify the grafting ratio, taking advantage of the differences in thermal stability between the grafted organic components and carbon framework. Mass spectrometry of the evolved gases confirmed the identity of the specific grafted species (Fig. 3b–e). The AR-GNPs showed a continuous weight loss during the TGA experiment, attributed to volatile impurities and the decomposition of oxygen-containing functional groups generated during the original

Table 1 A summary of mechanical properties of AR-, TTC- and TFI-SLG

Sample	Young's modulus (TPa)
AR-SLG	1.2 ± 0.4
TTC-SLG	1.4 ± 0.1
TFI-SLG	1.3 ± 0.2

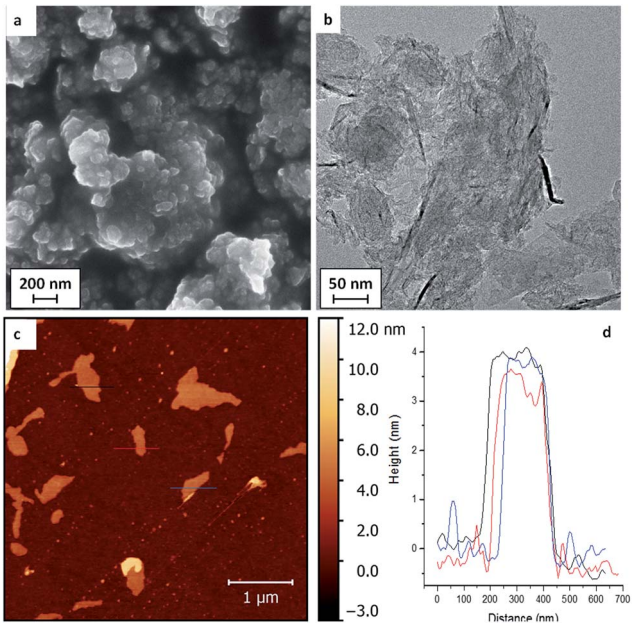

Fig. 2 (a) SEM, (b) TEM, (c) AFM images of the as-received GNPs, and (d) the height profile of AFM image.

synthesis, resulting in a 7.1 wt% loss at the final temperature of 850 °C. The TTC-GNPs displayed a smaller weight loss (2.4 wt%) than the AR-GNPs, as the volatile impurities are removed during the thermal treatment. XPS (see below) confirmed that the surface oxide groups decrease in concentration after thermal treatment. 1-Iodododecane (IDD) grafted GNPs (IDD-GNPs) showed a grafting ratio of 1.7 wt%, relative to TTC-GNPs; the grafted hydrocarbon chains (*m*/*z* 29 and *m*/*z* 85), but no iodide groups (*m*/*z* 127) or unreacted IDD (*m*/*z* 169), were observed by TGA-MS analysis. The grafting concentration (μmol of grafted functionalities per gram of GNPs), and hence the accessible radical site concentration, was therefore estimated to be 102 μmol g^{-1}, assuming a 1 : 1 reaction between the IDD and radicals. Previously, a range of nanotube materials have shown IDD grafting ratios in the range 1.4 wt% to 3.3 wt%, or 87 μmol g^{-1} to 202 μmol g^{-1}, (refer to ESI Table S1†);[23,24] the specific grafting density (normalised by specific surface area) was in a broadly similar range (around 0.4 μmol m^{-2}), indicating a similar surface concentration of defects. By comparison, the GNPs show a similar grafting ratio (1.7 wt%) to the other nanocarbons, but a slightly lower surface concentration of 0.16 μmol m^{-2}, which could be associated with relatively inaccessible slit-pore type sites at the flake edges. XRD of selected GNP samples confirmed that there was negligible change in the underlying platelet thickness; the lack of interlayer expansion is consistent with the expected functionalization of the accessible GNP surface (ESI Fig. S4 and Table S2†).[28,29] The grafting ratios (refer to Table 2) of P(MMA), P(4VP) and P(PEGMA) ranged from 3.7 wt% to 13.1 wt%, mainly reflecting the molecular weight of the grafting monomer; the PEGMA grafting ratio was relatively high due to the larger mass of the monomer, as previously observed on nanotubes.[23,24] Interestingly, the degree of oligomerisation is very similar (*ca.* 4 repeating units) across different

Table 2 Overview of AR- and various functionalised GNPs, in terms of grafting ratio (wt% grafted relative to the carbon nanomaterial framework), grafting concentration (μmol of grafted reagents per gram of carbon), monomeric repeats estimated number of monomer units in each grafted polymer/oligomer chain, atomic ratio determined by XPS analysis, maximum water solubility (μg mL^{-1}), I_D/I_G and I_{2D}/I_G values obtained from Raman spectroscopy

Sample	M_w	Grafting ratio (wt%)	Grafting concentration (μmol g^{-1})	Monomeric repeats	Atomic ratio (%)			Water dispersability (μg mL^{-1})	I_D/I_G ratio	I_{2D}/I_G ratio
					C	O	N			
AR-GNPs	N/A	N/A	N/A	N/A	93.2	6.3	0.5	191.5	0.97 ± 0.27	0.30 ± 0.25
TTC-GNPs	N/A	N/A	N/A	N/A	97.4	2.2	0.4	145.2	1.04 ± 0.09	0.38 ± 0.03
IDD-GNPs	169.3	1.7	102	1.0	95.3	4.2	0.5	113.6	1.04 ± 0.01	0.43 ± 0.01
P(MMA)-GNPs	100.1	3.8	384	3.8	93.2	6.6	0.2	79.0	0.99 ± 0.19	0.42 ± 0.23
P(4VP)-GNPs	105.1	4.4	417	4.1	94.7	1.5	3.7	523.4	0.96 ± 0.17	0.43 ± 0.17
P(PEGMA)-GNPs	518.6	15.1	285	2.8	89.4	10.6	0.0	734.7	1.07 ± 0.07	0.41 ± 0.24

types of nanocarbons (refer to ESI Table S1†). It seems that the polymerisation process is rather similar for different nanocarbons, leading to similar oligomer chain lengths. In these estimates, the termination of oligomerisation/polymerisation was assumed to occur readily at any point of the GNP surface rather than requiring another radical site; such an assumption is also consistent with the low degree of polymerisation. Preliminary data show that thicker GNPs from the same supplier (grade GM5) have a lower absolute degree of functionalization (ESI, Fig. S5 and S6†), as expected, in line with their lower accessible surface area.

The surface atomic ratios measured by X-ray photoelectron spectroscopy (XPS) analysis also confirmed successful grafting (Table 2). The heat treated control (TTC-GNPs) displays a reduced oxygen content (2.2%) compared to the original AR-GNPs (6.3%), due to the expected decomposition and rearrangement of the oxide groups; some groups are expected to be eliminated entirely,[30] but in other cases, radicals formed at high temperature re-trap oxygen on exposure to atmosphere at room temperature to form oxygen-containing pyrones and other species.[13,30,31] For the samples grafted with oxygen-containing polymers, P(MMA)- and P(PEGMA)-GNPs, the oxygen atomic ratio was significantly increased compared to AR- and TTC-GNPs, as expected. The clearest evidence of grafting can be seen in the P(4VP) samples, since they introduce a unique nitrogen signal. The nitrogen (N) atomic ratio was significantly increased (3.7%), compared to TTC-GNPs (0.4%) (further discussion in the ESI†).

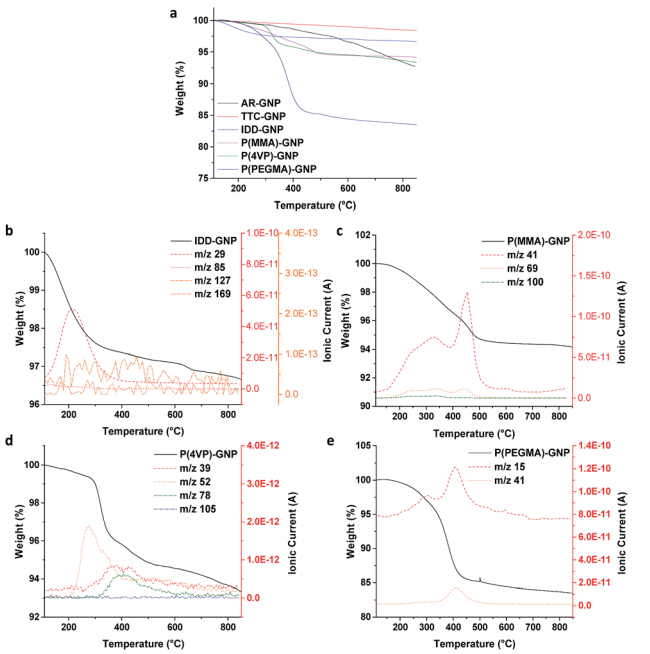

Fig. 3 TGA-MS profile for AR-, TTC- and various f-GNPs. Measurements were carried out under N_2 atmosphere.

The Raman spectra of the GNPs (Table 2 and Fig. S3†), show a broadly consistent I_D/I_G, within uncertainty, showing no evidence of damage during grafting. Although this ratio is not a very sensitive indicator when it is near unity,[32] a constant defect concentration is consistent with the proposed reaction mechanism, taking place only on the pre-existing defects. Similarly consistent Raman data have been found across a range of nanocarbons.[23,24] The slightly increased I_{2D}/I_G values indicate that the crystallinity of the GNPs was improved after thermal treatment, due to the removal of amorphous residue and/or some healing of the framework during the thermal activation treatment.

Dispersibility tests were carried out, by bath sonicating GNP samples in HPLC water for 5 minutes (an initial 1 mg mL^{-1} loading was previously found to be sufficient to ensure saturation). The dispersions were left to stand overnight and then the supernatants were carefully decanted in order to quantify the concentration by UV-Vis spectrometry. The AR-GNPs can be readily dispersed at 191.5 μg mL^{-1}, due to the high volume of surface oxides produced during the synthesis. The f-GNPs can be stably dispersed in water at a wide range of concentrations, from 79.0 to 734.7 μg mL^{-1}, driven by the various hydrophilicities of the grafted functionalities. The hydrophobic PMMA grafted sample was less dispersible than the AR-GNPs, as expected, with a concentration of 79.0 μg mL^{-1}; but notably the P(PEGMA)-GNP with the highly hydrophilic PEG chain, increased the dispersibility very significantly, reaching over 700 μg mL^{-1}.

Experimental

Monolayer graphene was grown *via* low-pressure CVD using methods detailed in previous reports.[16,25] CVD graphene was

then transferred to custom-made silicon nitride perforated membrane TEM grids, obtained from Silson, using methods detailed previously.[16] The GNPs were xGnP® Grade C with 750 $m^2 g^{-1}$ surface area, purchased from XG Sciences, Inc. (MI, USA, GC-750). All chemicals were purchased from Sigma-Aldrich and grafting reagents were purified through a neutral and basic aluminium oxide chromatographic column and degassed by bubbling N_2 gas for at least 30 minutes. Further details of the general thermochemical processing reaction procedures can be found in previous reports.[22–24,26] Graphene TEM grids were activated under vacuum ($<10^{-5}$ mbar, generated by a Edward Turbo pump station) at 850 °C in a quartz tube for 2 hours, and were allowed to cool down to room temperature, before exposing to the vapor of TFI (generated from 5 mL of injected TFI liquid) for 12 hours. The excess TFI was removed under vacuum ($<10^{-5}$ mbar) for 12 hours, until the weight of the grid remained constant. The bulk GNPs (100 mg) were activated at 1000 °C for 2 hours before cooling at room temperature, using bespoke glassware to avoid air exposure. The activated GNPs (100 mg) were soaked in the various grafting reagents (8 mL) overnight, identically to previous MWCNT and CB reactions. The excess monomers were removed by three cycles of 15 minute bath sonication (80 W, 45 kHz) and vacuum filtration.[25,26]

For HR-TEM, a JEOL ARM 200F was used, operating at 80 kV, with CEOS probe and image aberration correction. The dose was measured through the screen and was adjusted to $\approx 100\ e^-$ $Å^{-2}\ s^{-1}$ for high magnification imaging. AFM force curves were acquired with an Asylum Research MFP-3D-SA using methods outlined by Lee *et al.*[27] Multislice simulations were performed using spherical aberration −1 μm and defocus −20 nm (as measured for imaging). Simulations were performed using clTEM, an open-source multislice simulation package (M. A. Dyson, clTEM: OpenCL TEM/STEM simulation code, 2014). The multislice technique involves sectioning the structure that is to be simulated into thin slices normal to the direction of incidence of the electron beam. Then, the interaction between the incident electron wavefunction and one such thin slice can be modelled by multiplying the wavefunction with the transmission function obtained using only those atoms present in the thin slice. The wavefunction arriving at the sample is recursively multiplied by thin-slice transmission functions and then propagated through the sample to the next thin slice using Fresnel propagator functions modelling diffraction in a vacuum. The wavefunction propagating from the rear of the sample is the exit-wave, and a simulated image of this may be formed through convolution with a transfer function modelling the objective lens in the TEM, including its associated aberrations such as defocus, astigmatism, and spherical aberration. Alternatively, simulated diffraction patterns can be obtained by propagating the exit-wave *via* Fresnel diffraction to the imaging plane.[25,33–35]

SEM was performed on a LEO Gemini 1525 machine. Bright field TEM imaging was carried out using a JEOL2000 TEM, operating at 200 kV. AFM images were taken on a Nanoscope IV Digital Instruments AFM intapping mode. TGA-MS was performed using a Mettler TGA/DSC 1 coupled with a Hiden HPR-20 QIC R&D mass spectrometer. 5.0 ± 0.5 mg sample was heated from 30 °C to 100 °C at a ramping rate of 30 °C min^{-1} under N_2 atmosphere (with a continuous flow rate of 100 sccm). The specimen was then heated from 110 °C to 850 °C at a 10 °C min^{-1} ramping rate. For dispersibility tests, GNPs were bath sonicated for 15 minutes (45 kHz, 80 W) in HPLC water, with an initial loading of 1 mg mL^{-1}. The dispersed samples were left to stand overnight to allow the aggregates to settle. The supernatant concentration was determined by UV-Vis spectroscopy. Raman maps were obtained on a Renishaw InVia Confocal Raman spectrometer, using a green excitation laser (wavelength 532 nm, intensity 5%, scan time 30 seconds) under StreamlineTM mode (1800 lines per mm diffraction grating, at least 100 spectra taken for each sample). XPS spectra were recorded using a K-Alpha$^+$ instrument equipped with an MXR3 Al Kα monochromated X-ray source ($E = 1486.6$ eV). X-ray gun power was set to 72 W (6 mA and 12 kV). Charge compensation was achieved using the FG03 flood gun using a combination of low energy electrons and the ion flood source. Argon etching of the samples was applied using the standard EX06 Argon ion source using 500 V accelerating voltage and 1 μA ion gun current. Survey scans were acquired using 200 eV pass energy, 1 eV step size and 100 ms dwell times. All high resolution spectra were acquired using 20 eV pass energy, 0.1 eV step size and 1 s dwell times. Samples were prepared by pressing the sample onto carbon based double sided tape. The pressure during data acquisition was $\leq 10^{-8}$ mbar. XRD was carried out using a PANalytical X'Pert^3 PRO diffractometer operating at 40 kV and 40 mA. Dried powder samples were mounted onto a zero-background Si sample holder (PANalytical Ltd., UK). The diffractogram was recorded at a scan rate of 0.09° s^{-1} with the Cu K_α ($\lambda = 1.542$ Å) line, in the 2θ range from 5° to 60°.

Conclusions

Thermochemical functionalisation was successfully applied to both single-layer graphene and bulk commercially-available GNPs. Functionalisation of pre-prepared graphene TEM grids allowed direct imaging of the covalently-grafted functional group attached to an otherwise highly crystalline layer. AFM nano-indentation analysis of the single layer graphene confirmed there is no significant damage to the carbon framework during the thermochemical processing.[36] The degree of functionalization is significantly below that expected to disrupt the distinctive graphene band structure.[16] The extension to bulk CVD-grown GNPs demonstrates the versatility of the functionalisation. The approach can be applied to modify the accessible surfaces of both substrate-supported graphenes and bulk GNP powders using existing CVD furnace infrastructure, and should be straightforward to scale to large quantities. It should also be applicable to graphene based aerogels and other constructs. Although carried out under vacuum in the current experiments, the activation is also expected to work under nitrogen,[22] and at lower temperatures with varying degrees of functionalisation.[26] Interestingly the same method can be applied to essentially all sp^2 hybridised nanocarbons, with a degree of functionalisation that depends on defect concentration and available surface

area. The radical chemistry is very generic and readily applicable to a wide range of chemicals. Carbon framework damage, and the associated property degradation is minimised through the use of existing defects, and the relatively low degree of functionalisation introduced. Nevertheless, the degree of functionalisation has shown to be sufficient to modify dispersibility and other surface chemical properties of interest.[23,24] The solvent-free methodology discussed in this paper provides an alternative, generic, clean, robust and versatile strategy to functionalise graphene and related materials, complementing the existing liquid-phase and plasma processing approaches.

Acknowledgements

SH & MS acknowledge NIEHS (grant# U19ES019536) for the funding of this project. ZPLL thanks the EPSRC for support through a studentship (EP/M506679/1). HSL acknowledges the EU FP7-NMP Project MATFLEXEND (#604093), NR and HA acknowledge the EPSRC (EP/G007314/1). However, the views expressed in this paper are solely of the authors and do not necessarily reflect those of the funding agencies.

Notes and references

1 A. K. Geim, *Science*, 2009, **324**, 1530–1534.
2 Y. W. Zhu, S. Murali, W. W. Cai, X. S. Li, J. W. Suk, J. R. Potts and R. S. Ruoff, *Adv. Mater.*, 2010, **22**, 3906–3924.
3 K. S. Novoselov, V. I. Falko, L. Colombo, P. R. Gellert, M. G. Schwab and K. Kim, *Nature*, 2012, **490**, 192–200.
4 Y. Si and E. T. Samulski, *Nano Lett.*, 2008, **8**, 1679–1682.
5 E. Aram, M. Ehsani, H. A. Ithonakdar, S. H. Jafari and N. R. Nouri, *Fibers Polym.*, 2016, **17**, 174–180.
6 Y. L. Li, C. F. Kuan, C. H. Chen, H. C. Kuan, M. C. Yip, S. L. Chiu and C. L. Chiang, *Mater. Chem. Phys.*, 2012, **134**, 677–685.
7 J. D. Fowler, M. J. Allen, V. C. Tung, Y. Yang, R. B. Kaner and B. H. Weiller, *ACS Nano*, 2009, **3**, 301–306.
8 L. T. Duy, T. Q. Trung, V. Q. Dang, B. U. Hwang, S. Siddiqui, I. Y. Son, S. K. Yoon, D. J. Chung and N. E. Lee, *Adv. Funct. Mater.*, 2016, **26**, 4329–4338.
9 V. Georgakilas, M. Otyepka, A. B. Bourlinos, V. Chandra, N. Kim, K. C. Kemp, P. Hobza, R. Zboril and K. S. Kim, *Chem. Rev.*, 2012, **112**, 6156–6214.
10 C. W. Lai, Y. Sun, H. Yang, X. Q. Zhang and B. P. Lin, *Acta Chim. Sin.*, 2013, **71**, 1201–1224.
11 M. Quintana, J. I. Tapia and M. Prato, *Beilstein J. Nanotechnol.*, 2014, **5**, 2328–2338.
12 D. Chen, H. B. Feng and J. H. Li, *Chem. Rev.*, 2012, **112**, 6027–6053.
13 A. Bagri, C. Mattevi, M. Acik, Y. J. Chabal, M. Chhowalla and V. B. Shenoy, *Nat. Chem.*, 2010, **2**, 581–587.
14 M. Acik, G. Lee, C. Mattevi, A. Pirkle, R. M. Wallace, M. Chhowalla, K. Cho and Y. Chabal, *J. Phys. Chem. C*, 2011, **115**, 19761–19781.
15 T. Morishita, A. J. Clancy and M. S. P. Shaffer, *J. Mater. Chem. A*, 2014, **2**, 15022–15028.
16 A. J. Marsden, P. Brommer, J. J. Mudd, M. A. Dyson, R. Cook, M. Asensio, J. Avila, A. Levy, J. Sloan, D. Quigley, G. R. Bell and N. R. Wilson, *Nano Res.*, 2015, **8**, 2620–2635.
17 X. F. Gao, J. Jang and S. Nagase, *J. Phys. Chem. C*, 2010, **114**, 832–842.
18 P. V. Kumar, N. M. Bardhan, G. Y. Chen, Z. Y. Li, A. M. Belcher and J. C. Grossman, *Carbon*, 2016, **100**, 90–98.
19 I. Walters and M. Williams, Particulate Materials, Composites Comprising Them, Preparation And Uses Thereof, US 20130320274 A1, US 13/992,201, 2013.
20 A. Kumar, B. Behera and S. S. Ray, *RSC Adv.*, 2015, **5**, 39474–39481.
21 S. P. Economopoulos, G. Rotas, Y. Miyata, H. Shinohara and N. Tagmatarchis, *ACS Nano*, 2010, **4**, 7499–7507.
22 R. Menzel, M. Q. Tran, A. Menner, C. W. M. Kay, A. Bismarck and M. S. P. Shaffer, *Chem. Sci.*, 2010, **1**, 603–608.
23 S. Chen, S. Hu, E. F. Smith, P. Ruenraroengsak, A. J. Thorley, R. Menzel, A. E. Goode, M. P. Ryan, T. D. Tetley, A. E. Porter and M. S. P. Shaffer, *Biomaterials*, 2014, **35**, 4729–4738.
24 S. Hu, S. Chen, R. Menzel, A. D. Goode, M. P. Ryan, A. E. Porter and M. S. P. Shaffer, *Faraday Discuss.*, 2014, **173**, 273–285.
25 J. M. Cowley and A. F. Moodie, *Acta Crystallogr.*, 1957, **10**, 609–619.
26 S. Hu, PhD thesis, Imperial College London, 2015.
27 C. Lee, X. Wei, J. W. Kysar and J. Hone, *Science*, 2008, **321**, 385–388.
28 H. Fujimoto, *Carbon*, 2003, **41**, 1585–1592.
29 B. K. Saikia, R. K. Boruah and P. K. Gogoi, *J. Chem. Sci.*, 2009, **121**, 103–106.
30 G. S. Szymański, Z. Karpiński, S. Biniak and A. Świątkowski, *Carbon*, 2002, **40**, 2627–2639.
31 C. M. Chen, in *Surface Chemistry and Macroscopic Assembly of Graphene for Application in Energy Storage*, Springer Berlin Heidelberg, Berlin, Heidelberg, 2016.
32 L. G. Cançado, A. Jorio, E. H. M. Ferreira, F. Stavale, C. A. Achete, R. B. Capaz, M. V. O. Moutinho, A. Lombardo, T. S. Kulmala and A. C. Ferrari, *Nano Lett.*, 2011, **11**, 3190–3196.
33 P. Goodman and A. F. Moodie, *Acta Crystallogr., Sect. A: Cryst. Phys., Diffr., Theor. Gen. Crystallogr.*, 1974, **30**, 280–290.
34 K. Ishizuka and N. Uyeda, *Acta Crystallogr., Sect. A: Cryst. Phys., Diffr., Theor. Gen. Crystallogr.*, 1977, **33**, 740–749.
35 E. J. Kirkland, *Image Simulation in Transmission Electron Microscopy*, Kavli summer school, Ithaca, N.Y., 2006, p. 14853.
36 A. Zandiatashbar, G.-H. Lee, S. J. An, S. Lee, N. Mathew, M. Terrones, T. Hayashi, C. R. Picu, J. Hone and N. Koratkar, *Nat. Commun.*, 2014, **5**, 318–3194.